

See discussions, stats, and author profiles for this publication at: <https://www.researchgate.net/publication/221823217>

Anisotropy on the Collective Dynamics of Water Confined in Swelling Clay Minerals

ARTICLE *in* THE JOURNAL OF PHYSICAL CHEMISTRY A · MARCH 2012

Impact Factor: 2.69 · DOI: 10.1021/jp201543t · Source: PubMed

CITATIONS

15

READS

40

4 AUTHORS, INCLUDING:



[Eric Ferrage](#)

Université de Poitiers

57 PUBLICATIONS 1,204 CITATIONS

SEE PROFILE



[Laurent J Michot](#)

French National Centre for Scientific Research

160 PUBLICATIONS 3,272 CITATIONS

SEE PROFILE

Anisotropy on the Collective Dynamics of Water Confined in Swelling Clay Minerals

M. Jiménez-Ruiz,^{*,†} E. Ferrage,[‡] A. Delville,[§] and L.J. Michot^{||}

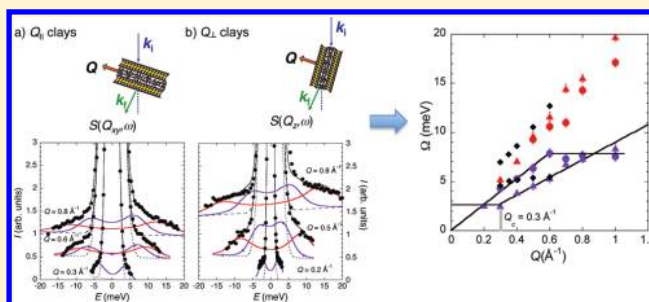
[†]Institut Laue Langevin, 6 Rue Jules Horowitz, BP. 156, F-38042 Grenoble Cedex 9, France

[‡]Institut de Chimie des Milieux et Matériaux de Poitiers, IC2MP-HydrASA, UMR7285-CNRS, Université de Poitiers, 86022 Poitiers Cedex, France

[§]Centre de Recherche sur la Matière Divisée, CNRS, Université d'Orléans FRE 3520, 45071 Orléans Cedex 2, France

^{||}Laboratoire Environnement et Minéralurgie, CNRS, Nancy Université UMR 7569 BP40 54501, Vandoeuvre Cedex, France

ABSTRACT: Collective excitations of water confined in the interlayer space of swelling clay minerals were studied by means of inelastic neutron scattering. The effect of bidimensional confinement on the dynamics of the interlayer water was investigated by using a synthetic Na-saponite sample with a general formula of $\text{Si}_{7.3}\text{Al}_{0.7}\text{Mg}_6\text{O}_{20}(\text{OH})_4\text{Na}_{0.7}$ in a bilayer hydration state. Experimental results reveal two inelastic signals, different from those described for bulk water with a clear anisotropy on the low-energy excitation of the collective dynamics of interlayer water, this difference being stronger in the perpendicular direction. Results obtained for the parallel direction follow the same trend as bulk water, and the effect of the confinement is mainly manifested from the fact that clay interlayer water is more structured than bulk water. Data obtained in the perpendicular direction display a nondispersive behavior below a cutoff wavenumber value, Q_c , indicating a nonpropagative excitation below that value. Molecular dynamics simulations results agree qualitatively with the experimental results.



1. INTRODUCTION

A large body of experimental and simulation work convincingly shows that the structure and dynamics of water are significantly modified when water molecules are close to interfaces or confined in porous spaces.^{1,2} Understanding the properties of such confined water is of prime importance in numerous scientific fields ranging from physics to biology, earth sciences, chemistry, and environmental sciences. In this latter domain, the case of water confined in the interlayer spaces of swelling clay minerals deserves particular attention due to its consequences on soil stability, plant nutrition, and elements cycling. Swelling clay minerals are layered aluminosilicate compounds ubiquitous in soils. They are formed with two tetrahedral layers (Si, Al, Fe) sandwiching one octahedral layer (Mg, Al, Fe) (TOT). This yields the TOT layer as shown in Figure 1a. Due to substitutions in either the tetrahedral or octahedral layer, the whole TOT layer bears a negative charge compensated by interlayer exchangeable cations whose valence and hydration properties control both swelling and colloidal behavior. The hydration of interlayer cations occurs in a stepwise manner as a function of water activity.^{3–5} The apparent interlamellar distance (d_{001}) then increases step by step from a value around 10 Å for the dry state to roughly 12.5 Å for the so-called monolayer state and then to 15.3 Å for the bilayer state. The domains of existence of the different hydration states, as well as the exact d_{001} value, strongly

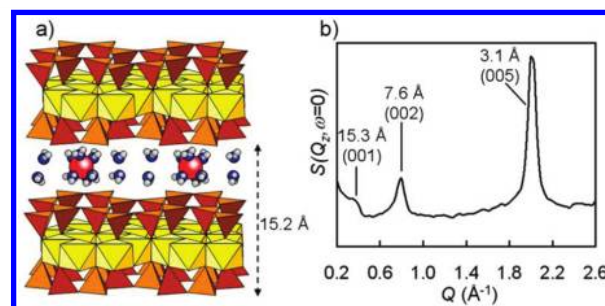


Figure 1. (a) Structure of swelling clay minerals. Tetrahedral and octahedral layers are shown in brown and yellow, respectively. Sodium, oxygen, and hydrogen in the interlayer space are shown in red, blue, and gray, respectively. (b) $S(Q, \omega = 0)$ pattern of oriented sample and associated (001) reflections.

depend on cation nature and on the amount and localization of charges in the TOT layer.^{6–14}

In such systems, the dynamical and structural properties of water can be considered as having the properties of a 2D confined fluid. As shown by the atomic density profile of interlayer species obtained from Grand-Canonical Monte Carlo

Received: February 16, 2011

Revised: January 27, 2012

Published: February 10, 2012

simulations in Figure 2, the system displays a strong confinement on the direction perpendicular to the clay layers,

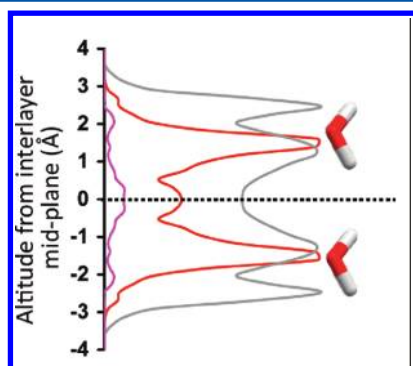


Figure 2. Atomic density profile of interlayer species obtained from Grand-Canonical Monte Carlo simulation showing the significant structuration of water molecules in the perpendicular direction to the clay layers. Sodium, oxygen, and hydrogen are shown in pink, red, and gray, respectively, whereas the interlayer midplane is shown as a dotted line.

inducing a specific structuration of water molecules. This structuration in turn impacts water organization in the parallel direction that is significantly different from that of bulk water.^{15–31} Such anisotropic organization is revealed by measurements and simulation of water diffusion in swelling clay interlayers that yield anisotropic diffusion coefficients significantly lower than that of bulk water.^{32–47}

These latter studies have mainly exploited the incoherent signal of hydrogenated water by Quasi-Elastic Neutron Scattering (QENS) or the collective motions via the density–density correlation (i.e., intermediate scattering function $F(Q,t)$) measured by means of Neutron Spin–Echo (NSE) experiments. In contrast, to our knowledge, the collective motions measured by coherent Inelastic Neutron Scattering (INS) on deuterated samples have not been studied so far in such clay–water systems. Using INS with a deuterated sample, the coherent scattering arising from the interference of the waves of different nuclei is measured, and therefore information about density fluctuations is obtained. The study of these collective motions is thus different from both self-motions of individual molecules obtained by incoherent QENS and slow collective motions obtained by NSE (see refs 48 and 49 for a general overview of the INS and QENS techniques).

As far as bulk water is concerned, inelastic neutron scattering,^{50–52} Inelastic X-ray Scattering (IXS),⁵³ and Molecular Dynamics (MD) simulations^{54,55} have already been used to analyze collective excitations. Two modes were described in these studies: the so-called “normal sound” and the high-energy excitation referred to as “fast sound”, the origin of the latter still being controversial. The “fast sound” was also measured in two-component liquids and gases with large atomic-mass difference^{56–59} and calculated on crystals composed of disparate mass particles^{60,61} as well as on polycrystalline ice.⁶² The effect of confinement on collective water dynamics has been studied by Sacchetti et al.,⁶³ who observed that normal vibrational modes of a water droplet coexist with collective excitations.

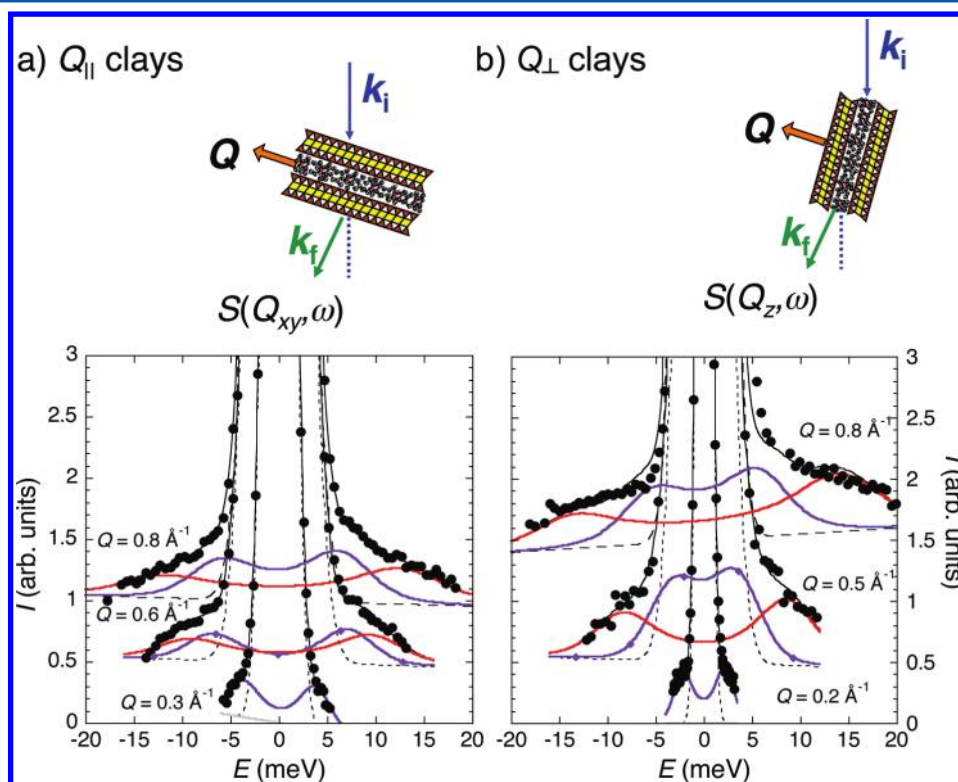


Figure 3. Upper frame: Scattering geometry for Q parallel to the clays, Q_{\parallel} (a), and Q perpendicular to the clays, Q_{\perp} (b). Lower frame: Several fitted spectra for the interlayer water at room temperature for Q_{\parallel} (a) and Q_{\perp} (b) to the clays. Experimental data are shown by solid symbols. The model intensities $I(Q,\omega)$ are depicted by the solid line. The resolution function is shown by the dashed line. The damped harmonic oscillators that take into account the low-energy and high-energy excitations appearing at the finite frequencies are shown by purple and red solid lines, respectively.

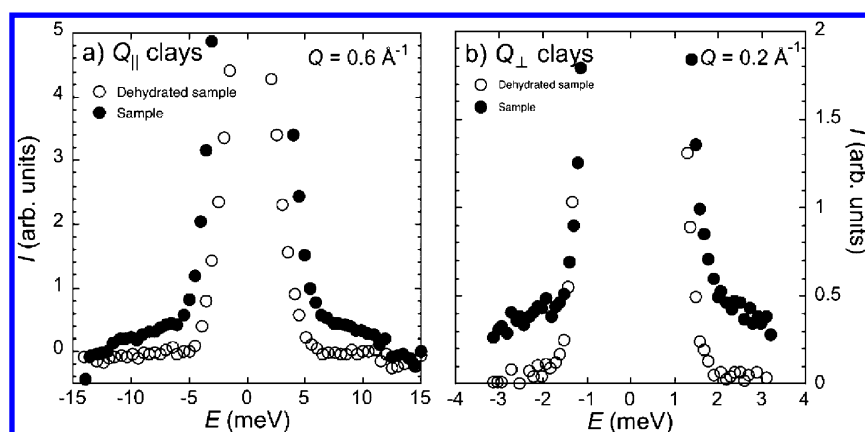


Figure 4. Comparison between the hydrated and dehydrated samples for Q_{\parallel} (a) and Q_{\perp} (b) to the clays for $Q = 0.6 \text{ \AA}^{-1}$ and $Q = 0.2 \text{ \AA}^{-1}$, respectively.

The present paper reports the study of the effect of bidimensional confinement on the collective motions of water molecules located in the interlayer of a synthetic Na-saponite sample by combining INS experiments and MD simulations. The synthetic saponite sample was chosen as it is devoid of mineralogical impurities, exhibits well-controlled swelling/hydration properties,^{13,64} and presents homogeneous chemistry, notably in terms of layer charge. Sample homogeneity is essential as numerical simulations are performed on a very limited clay volume, thus allowing a direct comparison of experimental and computational results. The anisotropy of the collective excitations was studied by means of a three-axis spectrometer (TAS), a very selective technique that allows aligning the momentum transfer vector, Q , parallel or perpendicular to the clay layers.

2. EXPERIMENTAL TECHNIQUES

The sample used in the present study is a synthetic saponite sample with a general formula of $\text{Si}_{7.3}\text{Al}_{0.7}\text{Mg}_6\text{O}_{20}(\text{OH})_4\text{Na}_{0.7} + n\text{D}_2\text{O}$. Details about the synthesis and crystal chemistry of the studied material can be found elsewhere.^{64,65} Oriented clay films of $\sim 15 \text{ }\mu\text{m}$ thickness were prepared by filtration of a Na-saturated clay suspension and stacked in a flat $6 \times 4 \times 0.4 \text{ cm}^3$ aluminum cell. The oriented clay stack of $\sim 3 \text{ mm}$ thickness was first dried at $80 \text{ }^\circ\text{C}$ in primary vacuum conditions ($\sim 10^{-3} \text{ Pa}$) and then equilibrated in deuterated water vapor environment at a relative humidity near 90%. Following this preparation, only interlayer water molecules are deuterated. Indeed, the H/D exchange of structural OH groups would require higher temperature or pressure conditions.⁶⁶ At 90% relative humidity the sample reaches a bilayer state with a d -spacing of 15.3 \AA that was checked by measuring the static structure factor as shown in Figure 1b.

The INS experiment was carried out on the thermal three-axis spectrometer IN8C, at the High Flux Reactor of the Institut Laue-Langevin (Grenoble, France). The optimal conditions yielding maximum flux and relatively high resolution in energy transfer were obtained using a Cu (200) monochromator and a Cu (111) analyzer. With a sample thickness of 3 mm , the measured sample transmission was 85%, and according to the corresponding scattering of 15%, the multiple scattering contribution can thus be neglected. Depending on the investigated Q -range, the experiment was carried out at different constant final wave-vectors, $k_f = 4.1 \text{ \AA}^{-1}$ (for $Q = 0.2 \text{ \AA}^{-1}$ on the perpendicular direction), 5 \AA^{-1} (for Q

$= 0.3$ and 0.4 \AA^{-1}), and 6 \AA^{-1} (for $Q = 0.5$ – 1 \AA^{-1}). The energy transfer range is then given by the energy and momentum transfer conservation laws for each Q and k_f . The energy resolutions measured at the elastic peak position using vanadium were fitted by a Gaussian function with full width half-maximum (FWHM) values of 1.27, 2.51, and 4.47 meV , respectively. The aluminum cell was placed inside a vacuum box, where the air pressure was lower than 10^{-4} mbar , to minimize additional scattering from surrounding air. Inelastic scans were then carried out at 300 K for wave vectors between 0.2 and 1 \AA^{-1} in two orientations (upper frame of Figure 3): parallel (Q_{\parallel}) and perpendicular (Q_{\perp}) to the clay layers. Sample hydration integrity was regularly checked by measuring $S(Q, \omega = 0)$ during the neutron scattering experiment.

In the sample under study, D atoms from interlayer species are ~ 5 times more numerous than H atoms from structural OH groups. Even considering that the scattering cross section of H is 10.5 larger than that of D, structural OH groups do not contribute significantly to inelastic spectra as shown on the spectra of the dehydrated sample (Figure 4). As far as the contribution of the TOT layer is concerned, clay samples are known to exhibit a rich vibrational spectrum in the energy range 20 – 140 meV ⁶⁷ that is outside the experimental energy range used for our study. In addition, phonon dispersion measurements on macroscopic crystals of dehydrated vermiculite,⁶⁸ whose structure is almost similar to saponite but with a higher charge and a regular layer stacking, revealed two acoustic branches, longitudinal and transverse (LA and TA), corresponding to the parallel and perpendicular direction to the clay layers, respectively. In the case of the saponite sample considered here, the organization of small individual clay particles in the parallel direction is disordered. The resulting lack of crystallographic order from particle to the adjacent ones suppresses the coherence on the inelastic signal, and as a consequence the TA branch (with an average energy of 5 meV) should not be present in our saponite sample. In the perpendicular direction, the clay lamellae are perfectly oriented, as shown in Figure 1b, and the LA branch should then in principle be present. However, due to the kinematic region reachable for our Q -value, the inelastic signal (10 meV for $Q = 0.3 \text{ \AA}^{-1}$) is outside the experimental window. Such an assumption is consistent with the spectra of dehydrated saponite (Figure 4) that does not exhibit any noticeable inelastic signal. The bump around 11 meV in Figure 4a is due

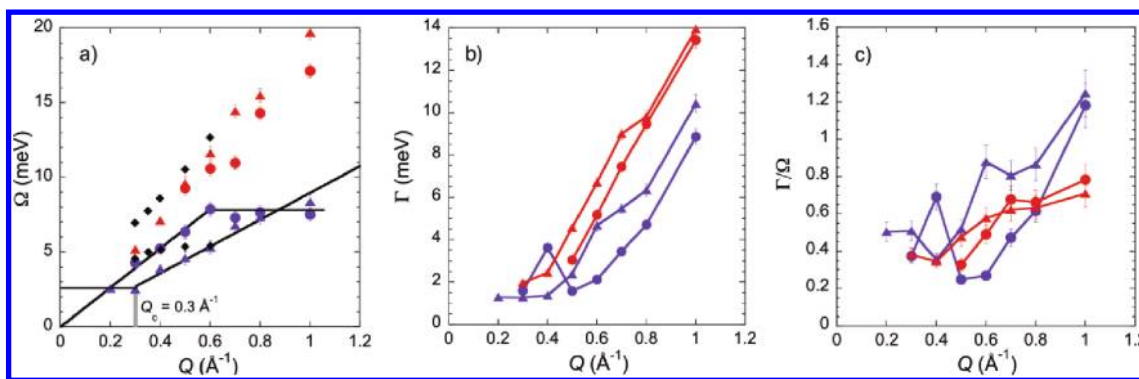


Figure 5. Q -dependence of (a) normalized frequency Ω , (b) damping parameter Γ , and (c) ratio Γ/ω , for the two inelastic signals obtained from the fitting of experimental spectra. Circles and triangles stand for directions parallel and perpendicular to the clay layers, respectively. Color code as Figure 3. In (a), the solid lines correspond to linear fits of the Q -dependencies in the dispersive regimes and are guides to the eye in the nondispersive regimes. Dispersion curves for bulk water are represented as solid diamonds and are taken from ref 51.

to a less precise empty cell subtraction for this dehydrated sample.

Under our experimental conditions, the INS signal is therefore highly dominated by interlayer water, and the influence of the dynamics of both structural OH groups and TOT layer can be neglected.

3. RESULTS AND DISCUSSION

3.1. Inelastic Neutron Scattering Experiment. After performing monitor normalization and cadmium subtraction, the intensity $I(Q, \omega)$ was measured in the direction parallel and perpendicular to the clay layers for various Q -values (Figure 3). Except in the perpendicular direction with $Q = 0.8 \text{ \AA}^{-1}$ where a Bragg peak appears, the inelastic signal accounts for $\sim 4\%$ of the total signal. It must be pointed out that the experimental energy range reached for each Q -value is different due to the kinematic conditions imposed by the neutron scattering experiment at very low Q -values. Shoulders clearly appear on both the Stokes and anti-Stokes sides of the central peak. To fit the complete profiles obtained, $I(Q, \omega)$ can be defined as

$$I(Q, \omega) \propto S(Q, \omega) \otimes R(Q, \omega) + \text{bcgr} \quad (1)$$

where $S(Q, \omega)$ is the dynamic structure factor and $R(Q, \omega)$ is the spectrometer resolution function given by

$$R(Q, \omega) = \frac{1}{\sqrt{2\pi}\sigma^2} \exp\left(-\frac{\omega^2}{2\sigma^2}\right) \quad (2)$$

where σ is the standard Gaussian deviation. The value of σ and the shape of the instrument function were calibrated using vanadium plates with the same geometry as the sample. The term bcgr corresponds to the background that is left as an adjustable parameter. The quantity $S(Q, \omega)$ encompasses all the information on liquid dynamics, including the elastic, quasi-elastic, and inelastic contributions. No quasi-elastic contribution that could broaden the central peak was considered in the present analysis since the quasi-elastic line is located inside the elastic peak due to the instrumental energy resolution used for the experiment. Therefore the signal outside the central peak was modeled as a purely inelastic component, $S_{\text{inel}}(Q, \omega)$.

In our first fitting attempt, we tried to model the inelastic signal using one damped harmonic oscillator (DHO) convoluted by the instrumental resolution.

$$S_{\text{inel}}(Q, \omega) = H(Q)n(\omega) \frac{4\omega\Omega^2\Gamma^2}{((\omega^2 - \Omega^2)^2 + 4\omega^2\Gamma^2)} \quad (3)$$

where $H(Q)$ is the strength of the single phonon excitation; $n(\omega) = [1 - e^{-\hbar\omega/k_B T}]^{-1}$ is the thermal occupation factor (k_B and \hbar stand for Boltzman and Planck constants, respectively); and Ω is the renormalized excitation frequency given by

$$\Omega^2 = \omega_s^2 + \Gamma^2 \quad (4)$$

where ω_s is the bare angular velocity of the oscillator and Γ is the damping parameter. This form is consistent with that predicted by generalized hydrodynamics. Such a treatment was clearly inefficient as some features of experimental data could not be reproduced. We then chose to model the inelastic signal as the sum of two DHOs, $S_{\text{inel}}(Q, \omega) = S_{\text{inel1}}(Q, \omega) + S_{\text{inel2}}(Q, \omega)$, i.e., without using a preimposed model for the fitting procedure. This model leads to the best χ^2 values and allows accounting for all experimental spectral features without using too many adjustable parameters. As shown in Figure 3, almost all experimental spectra except those obtained at the lowest Q -values ($Q = 0.2 \text{ \AA}^{-1}$) can be fitted using these two inelastic signals. This yields two components: a low-energy and a high-energy one, corresponding to the so-called "normal sound" and "fast sound", respectively.

Figure 5 displays the Q -dependence of the Ω parameter (Figure 5a) together with the evolution of the damping parameter Γ (Figure 5b) and that of the ratio Γ/Ω (Figure 5c), associated to the two inelastic signals used in the fitting procedure.

Concerning the High Frequency Excitation. The dispersion curves (Figure 5a) do not display any significant influence of confinement on the fast sound mode as the high-energy excitation behaves similarly as that observed in bulk water.⁵¹ Furthermore, Figure 5c shows equivalent Γ/Ω ratios for both directions, indicating the mainly isotropic character of the high frequency excitation.

Concerning the Low Frequency Excitation. *Parallel Direction (Q_{\parallel}).* The dispersion curve of the normal sound mode presents features similar to those observed for bulk water^{51–53} (Figure 5a): a dispersive behavior for low Q -values and a nondispersive for $Q \geq 0.6 \text{ \AA}^{-1}$. However, the energy value

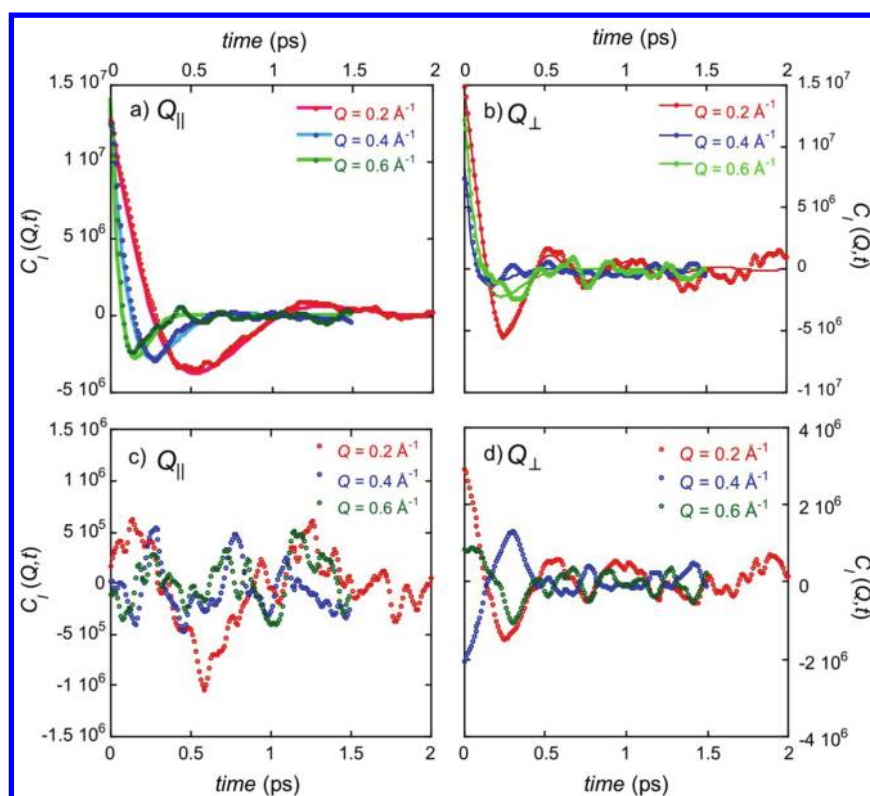


Figure 6. Autocorrelation function of the longitudinal current for the motion of all water molecules for Q_{\parallel} (a) and Q_{\perp} (b) to the clay surface for several Q -values. Continuous lines represent the fits to the DHO model. Lower frames show the autocorrelation of the longitudinal current for the motions parallel, Q_{\parallel} , (c) and perpendicular, Q_{\perp} , (d) to the clay surface for the water molecules pertaining to neighboring interlayers.

(8 meV) in the nondispersive Q -range is higher than the one found for bulk water (5 meV).^{51–53} It is worth pointing out that a similar trend has also been reported on the “fast sound” calculated for ice.⁶² Such an increase points toward the more structured nature of interlayer water, compared to bulk water. Indeed, near-infrared experiments carried out on the same clay minerals with a slightly higher charge and for the same water adsorbed amount have clearly revealed a network of interlayer water molecules more structured than that in bulk water.³¹

Perpendicular Direction (Q_{\perp}). The dispersion curve of the normal sound mode obtained in the perpendicular direction displays a significantly different Q -dependence. Indeed a crossover is observed for a Q -value of 0.3 \AA^{-1} . Below this value, a nondispersive behavior seems to be obtained. The extrapolation of this excitation to the center of the Brillouin zone ($Q \sim 0$) would give an excitation with an energy of ~ 3 meV. A nonzero value at $Q \sim 0$ is expected for confined acoustic or optic phonons and has been calculated on bidimensionally confined systems, for instance, Ar⁶⁹ and Si nanolayers,⁷⁰ whereas the behavior at higher Q -values reveals a dispersive nature of collective excitations. It must be pointed out that a Q -value of 0.3 \AA^{-1} corresponds to a distance in the real space of $\sim 20 \text{ \AA}$. Since the period of the clay/water interface is 15.3 \AA (see Figure 1b), the result suggests that density fluctuations can only propagate in the direction perpendicular to the clay surface between water molecules pertaining to the same or adjacent interlayers.

The Γ/Ω ratios in the parallel direction are the same as those reported for bulk water (0.7),⁶³ whereas they are slightly higher in the perpendicular direction. The low-energy excitation appears to be much more dependent on the orientation with respect to clay layers as results obtained in the parallel and

perpendicular directions are significantly different. A similar trend can be derived from Figure 5b where the classically observed quadratic evolution of Γ appears to be more affected by orientation for the low-energy excitation.

3.2. Molecular Dynamics Simulations. Due to the complex dynamical response of the system, classical MD simulations were performed to interpret the origin of such collective excitations. For that purpose, numerical simulations were performed for water molecules confined between four clay lamellae with a period of 15.3 \AA . Each lamella is composed of 84 unit cells. The corresponding size of the simulation cell was $63.84 \times 64.47 \times 61.16 \text{ \AA}^3$. The number of confined water molecules and their initial equilibrium configuration were first evaluated by Grand Canonical Monte Carlo (GCMC) simulations.^{19,31,43,71} After thermalization, we obtained 2883 confined molecules, corresponding to an average number of 9.5 confined water molecules per unit cell, in agreement with experimental data.^{13,19,64} The MD numerical simulations were performed for D_2O by using, as a starting point, one equilibrium configuration of the confined water molecules obtained by GCMC simulations. In these classical simulations, the water/water interactions are described by the SPC/E model, whereas ion/water interactions are described by an empirical potential compatible with the SPC/E water model.⁷² Clay/water and clay/ion interactions are described by an empirical potential⁷² recently modified¹⁹ to better describe the structure of confined water molecules. Due to substitution of Si atoms from the tetrahedral clay network by Al atoms, each clay lamella bears 60 elementary negative charges neutralized by interlayer sodium ions.

Before comparing these numerical data, obtained in the framework of classical physics, with experimental data, we must

first introduce the symmetrized form of the dynamic structure factor⁷³

$$S_{\text{class}}(Q, \omega) = S_{\text{sym}}(Q, \omega) = \frac{1 - \exp(-\hbar\omega/k_B T)}{\hbar\omega/k_B T} S_{\text{inel}}(Q, \omega) \quad (5)$$

In the case of the damped harmonic oscillator (DHO), the symmetrized form of the dynamic structure factor (see eq 3) becomes

$$S_{\text{sym}}^{\text{DHO}}(Q, \omega) = \frac{A}{2\pi} \left\{ \frac{\Gamma + (\omega + \omega_s) \tan \phi}{(\omega + \omega_s)^2 + \Gamma^2} + \frac{\Gamma + (\omega - \omega_s) \tan \phi}{(\omega - \omega_s)^2 + \Gamma^2} \right\} \quad (6)$$

with

$$\tan \phi = \frac{\Gamma}{\omega_s} \text{ and } \omega_s^2 = \Omega^2 - \Gamma^2 \quad (7)$$

The Fourier transform of this symmetrized form of the DHO structure factor leads to the symmetrized form of the Intermediate Scattering Function predicted by the DHO model

$$F_{\text{sym}}^{\text{DHO}}(Q, t) = \frac{1}{\cos \phi} \exp(-\Gamma|t|) \cos(\omega_s|t| - \phi) \quad (8)$$

which oscillates as a function of the angular velocity ω_s with the damping coefficient Γ and phase shift ϕ .

Information on the dynamical structure factor may then be obtained from the numerical simulations by analyzing the density fluctuations of the water molecules within the simulation cell.^{73,74} One may be tempted to evaluate the frequency spectrum of these density fluctuations, $S(Q, \omega)$,^{54,70} by calculating the FT of the intermediate scattering function $F(Q, t)$. However, for wave numbers smaller than 0.5 \AA^{-1} , the diffraction pattern evaluated from the molecular configurations within a finite simulation cell (size $\sim 60 \text{ \AA}$, see above) is totally masked by the density contrast induced by the empty surrounding. Therefore, we calculate the autocorrelation function of the longitudinal current^{73–75}

$$C_l(Q, t) = \langle J_l(\vec{Q}, 0) J_l^*(\vec{Q}, t) \rangle \quad (9)$$

with the longitudinal current given by

$$J_l(\vec{Q}, t) = \sum_{j=1}^{N_w} \sum_{\alpha=1}^3 b_{j\alpha} \frac{\vec{v}_{j\alpha}(t) \cdot \vec{Q}}{|\vec{Q}|} \exp(i\vec{Q} \cdot \vec{r}_{j\alpha}(t)) \quad (10)$$

where $b_{j\alpha}$, $v_{j\alpha}(t)$, and $r_{j\alpha}(t)$ stand, respectively, for the neutron scattering length, the velocity, and the position at time t of the atom labeled α within the molecule labeled j , and N_w is the total number of water molecules. The final autocorrelation functions plotted in Figures 6a,b are obtained by averaging at least 150 totally independent autocorrelation functions, each analyzing the trajectories of 2883 confined water molecules. Thanks to the complete lack of correlations between molecular velocities and positions,⁷⁴ the spatial correlations within such longitudinal current are short-ranged, avoiding the previously mentioned problem.

This autocorrelation function of the longitudinal current may be related to the Intermediate Scattering Function since^{74,75}

$$C_l(Q, t) = -\frac{1}{Q^2} \frac{d^2 F_{\text{sym}}(Q, t)}{dt^2} \quad (11)$$

By using eqs 8 and 11, we obtain

$$C_l^{\text{DHO}}(Q, t) = \frac{\exp(-\Gamma|t|)}{Q^2 \cos \phi} [\cos(\omega_s|t| - \phi)(\omega_s^2 - \Gamma^2) - 2\Gamma\omega_s \sin(\omega_s|t| - \phi)] \quad (12)$$

This relationship allows us to directly extract the dynamical parameters of the DHO model (i.e., Ω , the renormalized excitation frequency, and Γ , the damping factor) from the analysis of the autocorrelation function of the longitudinal current, in complete compatibility with the dynamical parameters extracted from the experimental data by using the same model (see above).

In addition to the autocorrelation of the longitudinal current evaluated for all water molecules contained in the simulation cell (Figure 6a,b), we also evaluated the autocorrelation between confined water molecules pertaining to neighboring interlayers, thus quantifying the occurrence of density fluctuations that can transfer between two adjacent interlayers. In the case of water motions parallel to the clay surface, such interlayer correlations remain negligible (Figure 6c), while significant correlations are detected for water motion perpendicular to the clay surface (Figure 6d), in agreement with previously mentioned conclusions (see Section 3.1). The initial values of the autocorrelation function of the longitudinal current quantifying these fluctuations between water molecules located within neighboring layers exhibit a net oscillation as a function of wavenumber (see Figure 6d). According to formulation of eqs 9 and 10, this behavior is not surprising since the products of the period of the clay interlayer (i.e., 15.3 \AA) by the investigated wave numbers ($Q \in [0.2, 1] \text{ \AA}^{-1}$) also oscillate around multiples of 2π .

Figure 7 shows the Fourier transform of the autocorrelation function of the longitudinal currents $C_l(Q, \omega) = FT(J_l(\vec{Q}, 0) J_l^*(\vec{Q}, t))$. From this expression, it is also possible to obtain the experimental dynamic structure factor $S(Q, \omega)$ as^{54,70}

$$S(Q, \omega) = (Q^2/\omega^2) C_l(Q, \omega) \quad (13)$$

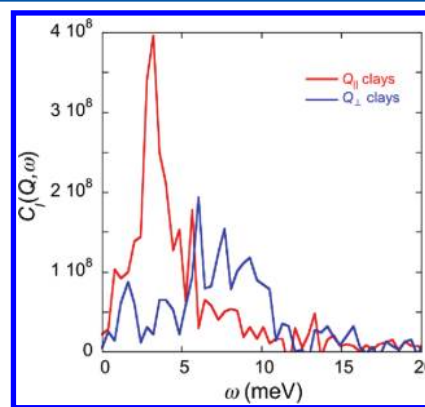


Figure 7. Fourier transform of the autocorrelation functions of the longitudinal current evaluated at $Q = 0.2 \text{ \AA}^{-1}$.

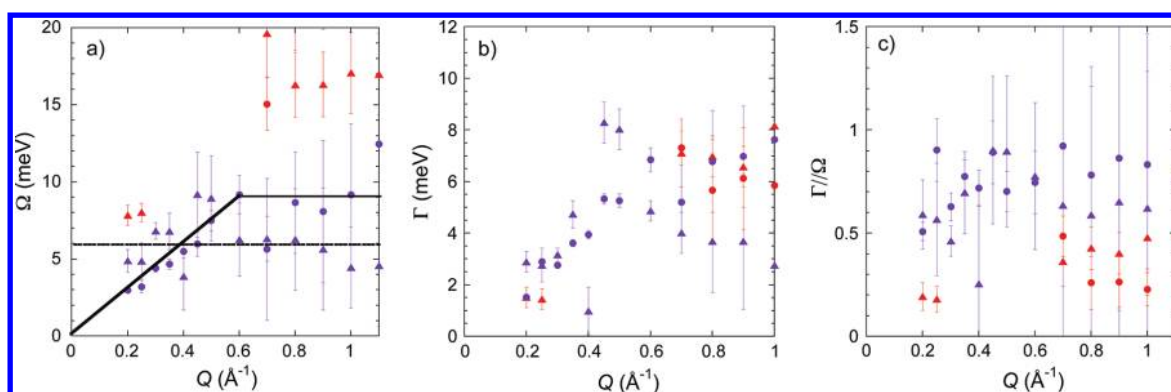


Figure 8. Q -dependence of (a) normalized frequency Ω , (b) damping parameter Γ , and (c) ratio Γ/Ω , obtained by fitting the autocorrelation function of the longitudinal current to the DHO model, for the two inelastic signals for water motion parallel and perpendicular to the clay surface. The symbols are the same as in Figure 5: circles and triangles stand for directions parallel and perpendicular to the clay layers, respectively.

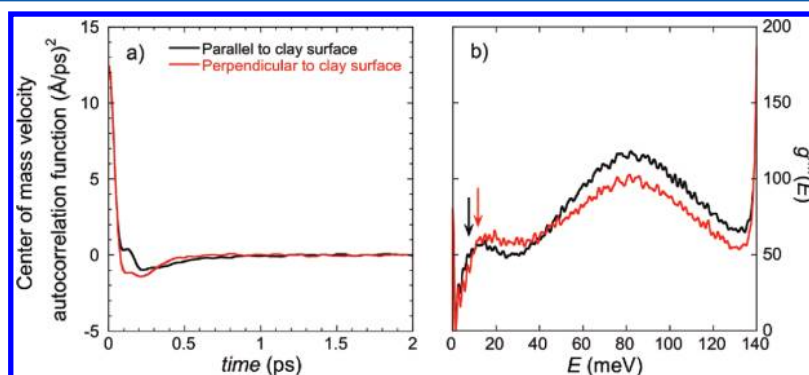


Figure 9. (a) Velocity autocorrelation functions of the water center of mass (see text). (b) "Neutron weighted" density of states, $g^{\text{nw}}(E)$. Black and red lines represent the results for Q parallel and perpendicular to the clays, respectively.

As displayed in Figure 7, all Fourier transforms of the autocorrelation functions of the longitudinal current perfectly cancel out at zero frequency because of the conservation of the total number of water molecules.^{54,74}

As displayed in Figures 6a,b, the DHO model (eq 12) satisfactorily reproduces the autocorrelation of the longitudinal current determined by MD simulations. When required (and generally for wave numbers larger than 0.6 \AA^{-1}), a second DHO describing the high-energy excitation is introduced to significantly improve the quality of the fit. Figure 8a displays the variation of the fitted normalized frequency (Ω) as a function of wavenumber. For water motions parallel to the clay surface, a quantitative agreement is obtained between the normalized frequencies Ω predicted by the MD simulations (Figure 8a) and those reported from experimental measurement (Figure 5a): in addition to the transition between dispersive and nondispersive regimes, that occurs at wave numbers $\sim 0.6 \text{ \AA}^{-1}$, the numerical simulations well reproduce the values of the normalized frequency excitation. By contrast, the agreement between numerical and experimental data is very poor for water motions perpendicular to the clay surface (see Figures 5a and 8a): while MD simulations predict a mainly nondispersive regime over the whole range of investigated wavenumbers, experimental data exhibit a dispersive branch for wavenumbers larger than 0.3 \AA^{-1} . Furthermore, the value of the normalized frequency reported for the plateau in Figure 8a ($6 \pm 3 \text{ meV}$) overestimates the experimental value ($\sim 3 \text{ meV}$) displayed in Figure 5a. These strong differences may be assigned to the limitations associated to the use of semi-empirical potentials in our MD simulations. As an example, a

r^{-12} power law is used by our model^{19,72} to reproduce the short-range clay/water repulsion, while an exponential law is certainly more appropriate. Furthermore, the model⁷² used to describe the stiffness of the clay lamellae requires probably some amendments. DFT quantum simulations should help us in improving these points. Finally, due to statistical noise, the complete extraction of the high-energy excitation is rather difficult to perform, accurately.

Values obtained by MD simulations for the damping factor (Figure 8b) semiquantitatively match experimental data (Figure 5b) for wave numbers smaller than 0.6 \AA^{-1} . For larger wave numbers, the experimental values of the damping factor still increase (Figure 5b), while MD simulations roughly predict a plateau (Figure 8b). Due to these discrepancies and the amplitude of the statistical noise, the values of the ratio Γ/Ω deduced from MD simulations (Figure 8c) are difficult to compare with the experimental data (Figure 5c).

Despite quantitative differences, both experiments and simulations reveal the existence of a nondispersive regime. To obtain complementary information, we tried evaluating the density of states (DOS). Unfortunately, the DOS is an ill-defined concept in a liquid since it refers to the density of normal modes per frequency. For that reason, we evaluated the Velocity Frequency Spectrum (VFS)⁷⁵ by a Fourier transform of the atomic velocity autocorrelation function. By contrast with isotropic liquids, even simple liquids confined between parallel lamellae exhibit a strong anisotropy of their velocity autocorrelation function (VAF).⁷⁶ This behavior is well reproduced in Figure 9a for the water mass center. Furthermore, the VAF may be used to determine the various

components of the self-diffusion tensor of such confined liquids⁷⁶

$$D_{\alpha,\alpha} = \lim_{t \rightarrow \infty} \int_0^t \langle \vec{v}_\alpha(0) \vec{v}_\alpha(\tau) \rangle d\tau \quad (14)$$

where $D_{\alpha,\alpha}$ is the eigenvalue of the self-diffusion tensor corresponding to the eigenvector labeled α . Due to the cylindrical symmetry of the confinement condition, two different eigenvalues are detected (see Figure 9a) corresponding to water diffusion in the directions parallel and perpendicular to the clay surface.⁷⁷ Water mobility along any direction is then derived from the two eigenstates by using⁷⁸

$$D_\theta = D_\perp \cos^2 \theta + D_\parallel \sin^2 \theta \quad (15)$$

where θ is the angle between the diffusion director and the normal to the clay surface. As a consequence, two components of the VFS are evaluated along the corresponding eigenstate of the water mobility. Finally, the neutron weighted VFS, $g^{\text{nw}}(E)$, was then calculated taking into account the different scattering lengths and mass of the components of the water molecule

$$g^{\text{nw}}(E) = 2 \left(\frac{\sigma_{\text{H}}^{\text{scatt}}}{M_{\text{H}}} g_{\text{H}}(E) \right) + \frac{\sigma_{\text{O}}^{\text{scatt}}}{M_{\text{O}}} g_{\text{O}}(E) \quad (16)$$

where σ_x^{scatt} is the scattering cross-section; M_x is the atomic mass; $g_x(E)$ is the partial VFS; and x relates to the different atoms of the molecule (H and O). The results obtained are shown in Figure 9b, where two main contributions to the VFS can be observed. The first one corresponds to translations at ~ 7 and 13 meV for the parallel and perpendicular direction, respectively. The second one is the wide libration centered around 80 meV. Both contributions appear shifted toward higher values and are wider with respect to the values of bulk water.⁷⁹ Indeed, for bulk water the translation is reported near 5 meV, significantly smaller than the value reported for the parallel (~ 7 meV) and perpendicular (~ 13 meV) directions, respectively. As far as librations are concerned, bulk water displays a contribution at ~ 61 meV, to be compared with positions of ~ 80 and 83 meV for our sample in the parallel and perpendicular direction, respectively. This shift of the translational contribution to higher energies and the increased signal broadening in the perpendicular direction result from the more significant confinement in that direction as illustrated in Figure 2. This behavior has also been observed on water confined in Vycor, where the translational peak appears much attenuated indicating the reduction of this degree of freedom upon confinement and an upshift of the librational peak indicating the hindrance of the librational motions by the presence of a surface. The low-energy excitation shown in Figure 8a clearly contributes to the first peak of the VFS. This confirms that the presence of a peak on the VFS arises from a dispersionless region on the dispersion curve.

3.3. Conclusions. In this paper, we have presented the first measurements on the anisotropy of the collective dynamics of water confined in a 2D system that evidence a clear anisotropy on the low-energy excitation of the collective dynamics of interlayer water. The collective excitations display a behavior significantly different from that of bulk water, this difference being stronger in the perpendicular direction. Data obtained in the perpendicular direction display a nondispersive behavior below a cutoff wavenumber value, Q_c , indicating a non-propagative excitation below that value. Results obtained for

the parallel direction follow the same trend as bulk water, and the effect of the confinement is mainly manifested from the fact that clay interlayer water is more structured than bulk water.

Despite the simplicity of the empirical potentials used in the present study, the results obtained by the MD simulations (i.e., dispersion curves and neutron weighted VFS) agree qualitatively with the experimental data.

Differences observed between the features of bulk water and those of clay interlayer water can be assigned to two effects: (i) the cations present in the interlayer space structure of the hydrogen bond network and (ii) the very limited interlayer spacing induces strong confinement. To discriminate between the influence of confinement and the influence of the presence of structuring cations, it would certainly be worthwhile to vary both parameters through a control of layer charge and relative humidity that also allow optimizing the potential used for MD simulations. Further studies, including Density Functional Theory calculations, could certainly address the influence of temperature and pressure on the dynamical features of interlayer water.

AUTHOR INFORMATION

Corresponding Author

*E-mail: jimenez@ill.fr.

Notes

The authors declare no competing financial interest.

ACKNOWLEDGMENTS

The authors wish to thank Dr. K. Schmalzl for stimulating discussions. The authors gratefully acknowledge financial support from European Marie-Curie Reintegration grant (contract no. MERG-CT-2007-046413) and from a French ANR "Jeunes Chercheurs" program (contract no. ANR-09-JCJC-0106-PorousClay). The authors wish to acknowledge two anonymous reviewers for their helpful comments.

REFERENCES

- (1) Brovchenko, I.; Oleinikova, A. *Interfacial and Confined Water*; Elsevier: New York, 2008.
- (2) Michot, L. J.; Villieras, F.; François, M.; Bihannic, I.; Pelletier, M.; Cases, J. M. *C. R. Geosci.* **2002**, 334, 611.
- (3) Bradley, W. F.; Grim, R. E.; Clark, G. F. *Z. Kristallogr.* **1937**, 97, 216.
- (4) Mooney, R. W.; Keenan, A. G.; Wood, L. A. *J. Am. Chem. Soc.* **1952**, 74, 1371.
- (5) Norrish, K. *Discuss. Faraday Soc.* **1954**, 18, 120.
- (6) Bérend, I.; Cases, J. M.; François, M.; Uriot, J. P.; Michot, L. J.; Masion, A.; Thomas, F. *Clays Clay Miner.* **1995**, 43, 324.
- (7) Cases, J. M.; Bérend, I.; François, M.; Uriot, J. P.; Michot, L. J.; Thomas, F. *Clays Clay Miner.* **1997**, 45, 8.
- (8) Sato, T.; Murakami, T.; Watanabe, T. *Clays Clay Miner.* **1996**, 44, 460.
- (9) Sato, T.; Watanabe, T.; Otsuka, R. *Clays Clay Miner.* **1992**, 40, 103.
- (10) Ferrage, E.; Lanson, B.; Sakharov, B. A.; Drits, V. A. *Am. Mineral.* **2005**, 90, 1358.
- (11) Cuadros, J. *Am. J. Sci.* **1997**, 297, 829.
- (12) Ferrage, E.; Lanson, B.; Sakharov, B. A.; Geoffroy, N.; Jacquot, E.; Drits, V. A. *Am. Mineral.* **2007**, 92, 1731.
- (13) Ferrage, E.; Lanson, B.; Michot, L. J.; Robert, J. L. *J. Phys. Chem. C* **2010**, 114, 4515.
- (14) Cabane, B.; Friedel, J. *J. Phys. (Paris)* **1971**, 32, 73.
- (15) Delville, A. *J. Phys. Chem.* **1993**, 97, 9703.
- (16) Chang, F. R. C.; Skipper, N. T.; Sposito, G. *Langmuir* **1995**, 11, 2734.

- (17) Chang, F. R. C.; Skipper, N. T.; Sposito, G. *Langmuir* **1997**, *13*, 2074.
- (18) Ferrage, E.; Lanson, B.; Malikova, N.; Plançon, A.; Sakharov, B. A.; Drits, V. A. *Chem. Mater.* **2005**, *17*, 3499.
- (19) Ferrage, E.; Sakharov, B. A.; Michot, L. J.; Delville, A.; Bauer, A.; Lanson, B.; Grangeon, S.; Frapper, G.; Jiménez-Ruiz, M.; Cuello, G. J. *J. Phys. Chem. C* **2011**, *115*, 1867.
- (20) Marry, V.; Turq, P.; Cartailier, T.; Levesque, D. *J. Chem. Phys.* **2002**, *117*, 3454.
- (21) Marry, V.; Turq, P. *J. Phys. Chem. B* **2003**, *107*, 1832.
- (22) Boek, E. S.; Coveney, P. V.; Skipper, N. T. *J. Am. Chem. Soc.* **1995**, *117*, 12608.
- (23) Boek, E. S.; Coveney, P. V.; Skipper, N. T. *Langmuir* **1995**, *11*, 4629.
- (24) Smith, D. E. *Langmuir* **1998**, *14*, 5959.
- (25) Shroll, R. M.; Smith, D. E. *J. Chem. Phys.* **1999**, *111*, 9025.
- (26) Greathouse, J. A.; Storm, E. W. *Mol. Simul.* **2002**, *28*, 633.
- (27) Skipper, N. T.; Sposito, G.; Chang, F. R. C. *Clays Clay Miner.* **1995**, *43*, 294.
- (28) Skipper, N. T.; Refson, K.; McConnell, J. D. C. *J. Chem. Phys.* **1991**, *94*, 7434.
- (29) Sposito, G.; Park, S. H.; Sutton, R. *Clays Clay Miner.* **1999**, *47*, 192.
- (30) Young, D. A.; Smith, D. E. *J. Phys. Chem. B* **2000**, *104*, 9163.
- (31) Rinnert, E.; Carteret, C.; Humbert, B.; Fragneto-Cusani, G.; Ramsay, J. D. F.; Delville, A.; Robert, J. L.; Bihannic, I.; Pelletier, M.; Michot, L. J. *J. Phys. Chem. B* **2005**, *109*, 23745.
- (32) Cebula, D. J.; Thomas, R. K.; White, J. W. *Clays Clay Miner.* **1981**, *29*, 241.
- (33) Poinsignon, C.; Estrade-Schwarzckopf, J.; Conard, J.; Dianoux, A. J. *Proceedings International Clay Conference Denver*, 1985; Schultz, L. G., Van Olphen, H., Mumpton, F. A., Eds.; The Clay Minerals Society: Bloomington, IN, 1987; p 284.
- (34) Tuck, J. J.; Hall, P.; Hayes, M. H. B.; Ross, D. K.; Poinsignon, C. *J. Chem. Soc., Faraday Trans.* **1984**, *80*, 309.
- (35) Tuck, J. J.; Hall, P.; Hayes, M. H. B.; Ross, D. K.; Hayter, J. K. J. *Chem. Soc., Faraday Trans.* **1985**, *81*, 833.
- (36) Poinsignon, C. *Solid State Ionics* **1997**, *97*, 399.
- (37) Swenson, J.; Bergman, R.; Howells, W. S. *J. Chem. Phys.* **2000**, *113*, 2873.
- (38) Swenson, J.; Bergman, R.; Longeville, S. *J. Chem. Phys.* **2001**, *115*, 11299.
- (39) Mamontov, E. *J. Chem. Phys.* **2004**, *121*, 9193.
- (40) Malikova, N.; Cadene, A.; Marry, V.; Dubois, E.; Turq, P.; Zanotti, J.-M.; Longeville, S. *Chem. Phys.* **2005**, *317*, 226.
- (41) Malikova, N.; Cadene, A.; Marry, V.; Dubois, E.; Turq, P. *J. Phys. Chem. B* **2006**, *110*, 3206.
- (42) Skipper, N. T.; Lock, P. A.; Tililoye, J. O.; Swenson, J.; Mirza, Z. A.; Howells, W. S.; Fernandez-Alonso, F. *Chem. Geol.* **2006**, *230*, 182.
- (43) Michot, L. J.; Delville, A.; Humbert, B.; Plazanet, M.; Levitz, P. *J. Phys. Chem. C* **2007**, *111*, 9818.
- (44) Malikova, N.; Cadene, A.; Dubois, E.; Marry, V.; Durand-Vidal, S.; Turq, P.; Breu, J.; Longeville, S.; Zanotti, J. M. *J. Phys. Chem. C* **2007**, *111*, 17603.
- (45) Burdallo, H. N.; Aldridge, L. P.; Churchman, G. J.; Gates, W. P.; Telling, M. T. F.; Kiefer, N.; Fouquet, P.; Setdel, T.; Kimber, S. A. J. *J. Phys. Chem. C* **2008**, *112*, 13982.
- (46) Malikova, N.; Longeville, S.; Zanotti, J. M.; Dubois, E.; Marry, V.; Turq, P.; Ollivier, J. *Phys. Rev. Lett.* **2008**, *101*, 265901.
- (47) Chakrabarty, D.; Gautam, S.; Mitra, S.; Gil, A.; Vicente, M. A.; Mukhopadhyay, R. *Chem. Phys. Lett.* **2006**, *426*, 296.
- (48) Price, D. L. *Curr. Opin. Solid State Mater. Sci.* **1997**, *2*, 477.
- (49) Price, D. L.; Saboungi, M. L.; Bermejo, F. J. *Rep. Prog. Phys.* **2003**, *66*, 407.
- (50) Teixeira, J.; Bellissentfunel, M. C.; Chen, S. H.; Dorner, B. *Phys. Rev. Lett.* **1985**, *54*, 2681.
- (51) Petrillo, C.; Sacchetti, F.; Dorner, B.; Suck, J. B. *Phys. Rev. E* **2000**, *62*, 3611.
- (52) Bermejo, F. J.; Alvarez, M.; Bennington, S. M.; Vallauri, R. *Phys. Rev. E* **1995**, *51*, 2250.
- (53) Sette, F.; Ruocco, G.; Krisch, M.; Masciovecchio, C.; Verbeni, R.; Bergmann, U. *Phys. Rev. Lett.* **1996**, *77*, 83.
- (54) Rahman, A.; Stillinger, F. H. *Phys. Rev. A* **1974**, *10*, 368.
- (55) Ricci, M. A.; Rocca, D.; Ruocco, G.; Vallauri, R. *Phys. Rev. A* **1989**, *40*, 7226.
- (56) Bosse, J.; Jacucci, G.; Ronchetti, M.; Schirmacher, W. *Phys. Rev. Lett.* **1986**, *57*, 3277.
- (57) Montfrooij, W.; Westerhuijs, P.; Dehaan, V. O.; Deschepper, I. M. *Phys. Rev. Lett.* **1989**, *63*, 544.
- (58) Enciso, E.; Almarza, N. G.; Dominguez, P.; Gonzalez, M. A.; Bermejo, F. J. *Phys. Rev. Lett.* **1995**, *74*, 4233.
- (59) Campa, A.; Cohen, E. G. D. *Phys. Rev. Lett.* **1988**, *61*, 853.
- (60) Enciso, E.; Almarza, N. G.; González, M. A.; Bermejo, F. J.; Fernández-Perea, R.; Bresme, F. *Phys. Rev. Lett.* **1998**, *81*, 4432.
- (61) Fernández-Perea, R.; Bermejo, F. J.; Martínez, J. L.; Enciso, E.; Verkerk, P. *Phys. Rev. E* **1999**, *59*, 3212.
- (62) Criado, A.; Bermejo, F. J.; Garcia Hernandez, M.; Martínez, J. L. *Phys. Rev. E* **1993**, *47*, 3516.
- (63) Sacchetti, F.; Orecchini, A.; Cunsolo, A.; Formisano, F.; Petrillo, C. *Phys. Rev. B* **2009**, *80*, 024306.
- (64) Michot, L. J.; Bihannic, I.; Pelletier, M.; Rinnert, E.; Robert, J.-L. *Am. Mineral.* **2005**, *90*, 166.
- (65) Pelletier, M.; Michot, L. J.; Humbert, B.; Barres, O.; D'Espinose de la Callerie, J. B.; Robert, J. L. *Am. Mineral.* **2003**, *88*, 1801.
- (66) Ferrage, E.; Martin, F.; Petit, S.; Pejo-Soucaille, S.; Micoud, P.; Fourty, G.; Ferret, J.; Salvi, S.; de Parseval, P.; Fortuné, J. P. *Clay Miner.* **2003**, *38*, 141.
- (67) Fan, Y.; Solin, S. A.; Kim, H.; Pinnavaia, T. J.; Neumann, D. A. *J. Chem. Phys.* **1992**, *96*, 7064.
- (68) Wada, N.; Kamitakahara, W. A. *Phys. Rev. B* **1991**, *43*, 2391.
- (69) Schmalzl, K.; Wallacher, D.; Koza, M. M.; Rheinstadter, M.; Strauch, D.; Knorr, K. *Eur. Phys. J.-Spec. Top.* **2007**, *141*, 117.
- (70) Donetti, L.; Gámiz, F.; Roldan, J. B.; Godoy, A. J. *Appl. Phys.* **2006**, *100*, 013701.
- (71) Allen, M. P.; Tildesley, D. J. *Computer Simulation of Liquids*; Clarendon Press: Oxford, 1994.
- (72) Cygan, R. T.; Liang, J. J.; Kalinichev, A. G. *J. Phys. Chem. B* **2004**, *108*, 1255.
- (73) Verkerk, P. *J. Phys.: Condens. Matter* **2001**, *13*, 7775.
- (74) Hansen, J. P.; McDonald, I. R. *Theory of Simple Liquids*; Academic Press: London, 1990.
- (75) Squires, G. L. *Introduction to the theory of Thermal Neutron Scattering*; Dover publications, Inc.: Mineola, NY, 1978.
- (76) Schoen, M.; Cushman, J. H.; Diestler, D. J.; Dhykerd, C. L. Jr. *J. Chem. Phys.* **1988**, *88*, 1394.
- (77) Porion, P.; Al-Mukhtar, M.; Faugère, A. M.; Pellend, R. J. M.; Meyer, S.; Delville, A. *J. Phys. Chem. B* **2003**, *107*, 4012.
- (78) Porion, P.; Rodts, S.; Al-Mukhtar, M.; Faugère, A. M.; Delville, A. *Phys. Rev. Lett.* **2001**, *87*, 208302.
- (79) Bellissent-Funel, M. C.; Chen, S. H.; Zanotti, J. M. *Phys. Rev. E* **1995**, *51*, 4558.